LAWRENCE
LIVERMORE
NATIONAL
LABORATORY

LLNL-JRNL-823571

Helium Bubble Growth Activation at Temperature in Implanted Aluminum

J. Hammons , S. Tumey, S. Aubry, Y. Idell, N. Bertin, R. Rudd, J. Jeffries, H. Lorenzana

June 16, 2021

Nature Materials

Disclaimer

Processes Controlling Helium Bubble Dynamics at Varying Temperatures in Simulated Radioactive Materials

Joshua A. Hammons[1]*, Scott J. Tumey[1], Sylvie Aubry[1], Robert E. Rudd[1], Yaakov Idell[1], Nicolas Bertin[1], Jan Ilavsky[2], Ivan Kuzmenko[2], Jason R. Jeffries[1] and Hector E. Lorenzana[1]

1. Physical and Life Sciences Directorate, Lawrence Livermore National Laboratory, 7000 East Avenue, Livermore, CA 94550, USA

2. X-ray Science Division, Argonne National Laboratory, 9700 S. Cass Avenue, Lemont, IL 60439, USA

Abstract

Alpha-radiation damage is known to degrade materials exposed to harsh radiation environments via swelling and embrittlement by nano-scale helium bubbles. How these bubbles grow under varying temperature is essential to understanding and predicting material failure and optimization. Using *in situ* X-ray scattering, we probed ≈ 10^{12} bubbles before, during and after annealing at different temperatures in He-implanted aluminum to reveal a critical growth activation temperature that depends strongly on the helium implantation conditions. An analysis of the data aided by our molecular dynamics simulations identifies multiple temperature-dependent bubble growth mechanisms above and below the critical growth activation temperature. Moreover, the irreversible bubble growth that occurs after annealing for ≈ 4 hr was evaluated using dislocation dynamics and found to negligibly affect the yield strength but may affect subsequent bubble growth at temperature. These *in situ* results provide valuable insight into bubble growth never observed before and reveal, for the first time, bubble shrinkage after cooling.

1. Introduction

Alpha radiation damage is known to damage materials through embrittlement[1], swelling[2] and surface blistering[3], and is a major concern in nuclear energy generation and storage, and perhaps future applications in space. All of these mechanisms that degrade the host material are caused by an increase in the number and size of "bubbles" within the host material that form as nascent helium-vacancy clusters, followed by growth via dislocation loop punching and coalesce[4]. Rational design of the next generation of materials for such applications will greatly benefit from accurate predictions of how the bubble morphology changes within a host material as the concentration of point defects[5] and helium increase with age. The aim of this study is to understand how the bubble growth kinetics at varying temperatures are affected by the initial bubble morphology (size and number) as well as different exposures to alpha particles, with a particular interest in gaining insight into the self-irradiating phenomena in plutonium.[6]

The accumulation of helium and damage to the crystal lattice during aging is simulated here with helium implanted aluminum, which has a similar bubble morphology and melting point as Pu, an important nuclear-energy power source. Additionally, aluminum is a common material that is not radioactive, thus minimizing safety concerns and eliminating complex contributions from other impurities often associated with radioactive decay, such as U and Am. While helium implantation has been used to study bubble morphologies in a broad range of metals, the implantation approach used here is optimized for small angle X-ray scattering[7], which is a bulk technique. Briefly, this implantation results in a relatively thick implanted region within the foil, whilst varying the helium concentration orthogonal to the ion beam. Two different samples of implanted Al were chosen here to investigate the dependance on the initial bubble morphology, which can be varied by implanting helium above and below the coulomb barrier of Al (7.1 MeV). In both cases, the bubble morphologies are similar to those found in Pu[6], with bubbles slightly larger (≈5 nm vs 3 nm) and low in number observed in the sample implanted below the coulomb barrier[7]. The implanted samples aim to represent aged plutonium with the major difference between the sample characteristics being the bubble morphology and damage incurred during implantation.

Some of the earliest *ex situ* experiments of implanted helium observed significant bubble growth in aluminum and change in the bubble morphology and number at 500 °C, whereas little change was observed up to 200 °C[8-10]. However, bubble growth kinetics as a function of temperature are difficult to quantify with transmission electron microscopy (TEM), where only a limited number of bubbles are counted and often only after the heat treatment. Therefore, in addition to TEM, *in situ* and *ex situ* small angle X-ray scattering (SAXS) are used in this study to evaluate a much larger number of bubbles in the samples before, during and after heating to quantify the dependence of bubble size distribution with temperature and time. The number density and size distribution of bubbles determined by SAXS are then used as input into dislocation dynamics simulations to evaluate the effect of the change bubble morphology on the bulk properties of the aluminum.

There are different mechanisms of bubble growth, which may occur simultaneously and difficult to deconvolute from experimental observations. Immediate bubble growth (on short time-scales)

occurs when an over pressure exists in the bubble, which punches out dislocation loops at the bubble-metal interface[11]. Increasing the temperature in an isochoric process would increase the pressure, and, at the same time, may also remove retained dislocation loops of adjacent bubbles, thereby allowing growth[11]. However, growth may not be a continuous function of temperature, as the threshold pressure for dislocation loop punching is higher for smaller bubbles[12], or because the vacancy influx to the bubble is much greater than the vacancy emission of the bubble. In the latter case, the rapid bubble growth is a strong function of the concentration of vacancies near the bubble[5], which will be higher in the sample implanted with a higher concentration of helium. Combined molecular dynamics and small-angle X-ray scattering (SAXS) experiments are used here to determine the extent to which bubbles are expected to grow on short time-scales. Continued bubble growth observed by SAXS at much longer time-scales is modeled assuming bubble-bubble interactions, such as Ostwald ripening[13] or migration-coalescence[14] to determine which mechanisms may dominate over longer times at temperature. In this way, the bubble growth mechanisms on short and long time-scales are resolved for two Al samples with different implantation conditions.

2. Materials and Methods

2.1 Helium-Implantation

Al Foils (GoodFellow, 0.125 mm, 99.999 % pure) were implanted with He at the Lawrence Livermore National Laboratory (LLNL) Center for Accelerator Mass Spectrometry (CAMS) (Fig. 1). Details of the implantation can be found in a previous publication, along with the initial characterization of the foils[7]. Two of the previously reported samples were annealed to resolve differences in the bubble dynamics with implantation conditions: 1) sample prepared with a He loading of 0.1 % and implantation thickness of 74 μm and 2) a He loading of 0.2 % and 37 μm implantation thickness. The thickest implantation yielded the most uniform and highest signal. However, He implantation energies above the coulomb barrier, >CB, for Al (7.1 MeV) were required to reach the back half of the sample with a 74 μm thickness. Both samples were implanted with helium from the back-side (high energies) to the front-side (low energies). Implantation energies above this threshold have been shown to increase the number density of bubbles[7]. Therefore, the second sample was implanted with He energies below the coulomb barrier, <CB. Implantation depths were calculated using the Stopping and Range of Ions in Matter (SRIM) code[15] and shown in Fig. 1b. Ion beams were tuned to produce an average beam current of ≈ 6 ions sec^{-1} and were defocused to produce an axially-symmetric 2D gaussian profile with a full-width-half-maximum (FWHM) of ≈ 4 mm to implant He over a 6 mm diameter area of the foil (Fig. 1c), as measured with a beam profile monitor (National Electrostatics Corporation).

Following the initial characterization[7], each sample was cut into four equal pieces for separate annealing and transmission electron microscope (TEM) experiments as shown in Fig. 1d. In this study, two of the four pieces from the 0.2 %, 37 μm implanted sample were evaluated by TEM and the remaining pieces were used for *in situ* annealing experiments as described below. The elapsed time between implantation and experiment varied between 1 month to 2 years and is noted below.

2.2 X-ray Scattering

The *in situ* annealing experiments were designed to evaluate the effect of both temperature and time on the bubble size and number. All *in situ* annealing experiments were performed at the USAXS/SAXS/WAXS beamline (9-ID-C) within the advanced photon source (APS) at Argonne National Laboratory. Samples were illuminated with monochromatic X-rays at 21 keV and the X-ray scattering was collected at three different *q*-ranges using the Bonse-Hart USAXS (10^{-4} $Å^{-1}$ to 0.3 $Å^{-1}$) instrument, a pinhole SAXS detector (0.03 $Å^{-1}$ to 1 $Å^{-1}$) and a WAXS detector (2 $Å^{-1}$ to 6 $Å^{-1}$)[16]. Exposure times used for the pinhole SAXS and WAXS detectors varied between (10 s to 100 s) and (20 s to 30 s), respectively. A beam size of 0.8 mm by 0.8 mm was used for the USAXS, while beam sizes of 0.4 mm (h) and 0.2 mm (v) were used for the SAXS/WAXS. Only the data collected from the pinhole SAXS detector are shown in the main text, due to the low signal-to-noise from some of the samples. The data obtained from the USAXS instrument did not always have the signal-to-noise required to analyze and can be found in the supporting information. All of the data was reduced and analyzed using the Indra, Nika and Irena packages for Igor Pro[17, 18].

2.3 Electron Microscopy

Two of the pieces from the Al foil implanted with 0.2 % He and 37 μm thickness (one sample was as-implanted while the other sample was annealed to 200 °C for two hours) were evaluated by a FEI 80-300 Titan TEM 1.5 years after implantation; the corresponding SAXS data from a separate piece of the same sample (Fig. 1c) was collected ≈ 2 months prior to TEM imaging. The TEM was operated at 300 kV providing a point-to-point resolution of 0.20 nm, which provides sufficient resolution to resolve all bubble sizes present in the material. The samples were prepared for TEM analysis through standard focused ion beam (FIB) lift-out using the FEI Nova 600 Dual-Beam, which was operated at 30 kV.

2.4 Annealing Experiments

The first samples evaluated were two pieces from the Al foil implanted with 0.1 % He and 74 μm thickness (>CB). The two pieces were placed in the Linkam stage as shown in Fig. 1e so that the X-ray aperture was within the FWHM of the He concentration gradient. In these first experiments, the SAXS from a non-implanted Al foil, within the Linkam stage, was subtracted from the foils as outlined in our previous publication[7]. Three separate pieces each were annealed at 200 °C (Fig. S1c), 500 °C (Fig. 2e) and 400 °C (Fig. S6) for four hours; the pieces annealed at 200 °C and 500 °C were ≈ 1 month after implantation and 400 °C was 7 months old. Importantly, all of these samples were as-implanted and did not undergo any prior heat treatment. During the annealing, all three *q*-ranges were collected every ≈ 7 minutes. The SAXS data was placed on an absolute scale by applying a scaling factor that resulted in overlap between the pinhole SAXS data and the calibrated USAXS data obtained during annealing at 500 °C where sufficient signal was obtained to combine the data.

In order to evaluate any change in the bubble heterogeneity and diameter after annealing, the spatial-resolved SAXS was obtained from samples annealed at 200 °C and 500 °C along with the other two as-implanted pieces at beamline 12-ID-B within the APS approximately 3 months after implantation. In these experiments, a monochromatic, 14 keV, X-ray beam of 0.2 mm by 0.2 mm

was used to collect the SAXS from every 0.2 mm by 0.2 mm area of each piece and across the entire implanted area. These four pieces, as well as a piece of non-implanted Al foil were mounted on a sample holder and the air scattering was used as a background subtraction. The variation in scattering from the non-implanted Al foil was evaluated and used to determine which features were unambiguously attributed to helium bubbles and which features could be attributed to variation in the grain heterogeneity in the Al. The absolute scattering intensity was not calibrated in these data and the intensity units are arbitrary.

Temperature ramp experiments were carried out on one of the pieces of Al that was implanted with a maximum concentration of 0.2 % and 37 μm thickness (<CB) and a previous implanted piece with a maximum concentration of 0.1 % and 74 μm thickness (>CB) that was annealed at 400 °C, where bubble growth was observed (Fig. S6); bubble growth was again observed at this temperature during the temperature ramp experiment. The elapsed time between implantation and the experiment on the 0.2 % and 37 μm thickness was 1.5 years and the time between prior annealing and the temperature ramp experiment on the 0.1 % and 74 μm thickness was also 1.5 years; approximately 2 years since implantation for this sample. These experiments were also performed at beamline 9-ID-C at the APS in a Linkam heating stage and with the same beamline configuration as the first annealing experiments. The purpose of these experiments was to observe if and how the bubble volume fraction and size changes at each temperature between 200 °C and 550 °C. The temperature ramp schedule was initiated by increasing the sample temperature from room temperature to 200 °C. After one hour at 200 °C, the sample temperature was increased to 300 °C for one hour, followed by another increase to 400 °C for an hour. From 400 °C, the sample temperature was increased in 50 °C increments up to 550 °C and held at each temperature for one hour; the final temperature was held at 550 °C. At each temperature, between two and four different positions on the sample were measured between the area where helium concentration is at its peak and up to 0.8 mm away. In each case, the scattering background from the empty Linkam stage was subtracted from these data as the background Al scattering was proven to not contribute to the high-q scattering where the bubbles dominate[7].

3. Theory and Calculations

3.1 Dislocation Dynamics (DD)

The dislocation dynamics, DD, method[19] is used to quantify the effects of implanted helium bubbles on the strength of aluminum metals. In this work, the Parallel Dislocation Simulator (ParaDiS) code[19] is used for dislocation dynamics simulations. In the ParaDiS code, the general curvilinear dislocation topology is discretized into a finite set of degrees of freedom represented by straight segments ended by nodes. Forces on dislocation line segments and nodes are calculated in an isotropic elastic media. The positions of these degrees of freedom are updated through equations of motion and a time integration algorithm. Since dislocation lines tend to multiply during DD simulations, procedures are defined for adaptively refining the discretization of the dislocation network, see details in Ref. [19]. Recently, the DD method has been extended to explicitly model the interactions between dislocations and defects other than dislocations. Several physical mechanisms can describe the interactions between dislocations and defects such as precipitates, voids, bubbles etc., a few of them are described in Ref. [20]. In this work, helium bubbles are defined as nondeformable spheres with an initial internal pressure.

The effect of pressure inside helium bubbles is modelled using the Eshelby stress[20]. When a dislocation meets a helium bubble, it feels the pressure inside the bubble through an added Eshelby force described in detail in Ref. [20]. Dislocation dynamics simulations require as input the mobility law of single dislocations of screw and edge character to model large ensemble of interacting dislocations. The molecular dynamics method is used to obtain these mobility laws and details can be found in the supporting information.

Dislocation dynamics simulations were performed on pure aluminum, and helium implanted aluminum before and during high temperature annealing using a 0.5 μm cubed simulation box under $5x10^6$/s strain rate tension loading in the [001] loading direction. An initial density of screw dislocations of $2x10^{15}/m^2$ was chosen so that all possible slip systems in the FCC lattice are present in the system at the beginning of the simulation while balancing the initial yield stress and the computational cost of the fully hardened simulation. To determine the overall effect of implantation, the number density and size distribution were obtained from modelling of SAXS data obtained before annealing at each temperature. Assuming a volume fraction of 0.001 reported previously for the unannealed system[7], about 24,000 bubbles were incorporated in the simulation of the implanted aluminum at 300K. In order to observe the effect of annealing, two additional simulations were performed at 770K with and without the large bubbles observed after annealing. As before, the size distribution and relative volume fraction were obtained from the SAXS modeling, which corresponded to ~ 15,000 small bubbles and ~ 60 of the larger bubbles. The size distributions used in each case can be found in the supporting information. The stress and the dislocation density were obtained at each strain and reported in Fig. 5.

3.2 Molecular Dynamics (MD)

Molecular dynamics, MD, simulations were used to simulate the formation of helium bubbles at room temperature and their growth as the temperature is increased. MD simulates the motion of atoms interacting via classical interatomic potentials[21, 22] here using the LAMMPS code[23]. Molecular dynamics (MD) techniques to simulate metals with voids[24-27] and helium bubbles[28-39] have been developed extensively. Applied to study a large range of phenomena including how helium flux affects bubble growth, the mechanical properties of metals with bubbles and the effect of bubbles on surface morphology, MD provides a detailed description of the processes occurring on short time and length scales. In addition to the interatomic potential, MD depends on the initial configuration (the microstructure) and boundary conditions like the flux of He into and out of the system. Most of the MD studies of bubbles have been in metals used in structural members in fission or fusion reactors, especially iron and tungsten and their alloys.

A system containing 7 million aluminum atoms in an fcc lattice was seeded with ~1 nm diameter cavities filled with liquid helium at ~1 GPa pressure. The number density of these proto-bubbles was chosen to match the number density obtained experimentally so that the relative distance of protruded dislocation loops can be observed; interacting dislocation loops may complicate the bubble growth. We note that in reality, bubbles can be either closer or further apart. In this case, following an initial period of thermal equilibration at a temperature of 300 K, the system was advanced in time using a time step of 0.2 fs in the NPH ensemble with a total system pressure of 0.2 GPa. Then helium atoms were added gradually over 300 ps remaining at the same

temperature, 300 K. At first, the additional He atoms induced a small elastic increase in the volume of the bubble. At a pressure of 5 GPa, the stress at the bubble surface induced the nucleation of dislocations. The bubble pressure was determined by matching the He-He radial distribution function (RDF) from the simulation to reference RDFs from fully periodic pure He simulations at fixed temperature and volume in which the pressure could be determined using the conventional virial formula. While the bubbles did not immediately nucleate prismatic loops, the dislocations emitted from the bubble surface had some prismatic character enabling the bubble volume to increase through plastic deformation. In most cases the dislocation loops remained attached to the bubble surface, although in a few cases a prismatic loop detached from the surface and moved away to a position between the bubbles. No cases of loops spanning the entire distance between bubbles were observed.

The temperature of the system was then ramped to 900 K. The increase in temperature induced additional dislocations to nucleate from the surface of the bubbles, with a concomitant increase in the volume of the bubble. The final pressure of the helium in the bubbles was 5.0 GPa greater than that of the surrounding aluminum. The bubble diameter was ≈4.2 nm, as determined from the volume occupied by the helium atoms. Again, we did not observe any cases of loops spanning the entire distance between bubbles.

We also increased the temperature to 1600K to induce Al melt and determined the over-pressure at a series of decreasing temperatures down to 950K. The over-pressure (Laplace pressure) was ≈0.7 GPa, and the corresponding surface tension was found to be 1.06 ± 0.05 J m^{-2} for this range of temperatures, as determined by the Young-Laplace formula. For comparison, the over-pressures at lower temperatures were 5.9 GPa (300K) and 5.8 GPa (800K), corresponding to effective surface tensions of 6.04 ± 0.06 J m^{-2} at both temperatures. These values are well above realistic surface tensions, indicating that the over-pressure is related to the strength, σ_{yield}, of the matrix material: $\Delta P = (2/3)\sigma_{yield}$. The corresponding strengths of ≈ 8.8 GPa are lower than the yield strengths observed in quasi-continuum aluminum void growth simulations for nanoscale voids (19.2 GPa tension, corresponding to σ_{yield} = 12.8 GPa at T=0 K)[39].

Simulations using the Mishin potential[40] for aluminum were also carried out to observe any dependence on potential. The results were very similar. This potential produced less point-defect debris (vacancies and interstitial atoms) than the Ercolessi-Adams potential[41]. There was also less tendency for the dislocation cores to split appreciably into partial dislocations spanned by a stacking fault ribbon. The size of the plastic zone and the size of the bubble as functions of temperature were very similar with the two potentials. The Ercolessi-Adams potential, for which snapshots were plotted in Fig. 3, was the potential used to calculate the dislocation mobility for input to the dislocation dynamics simulations.

3.3 SAXS Modelling

The SAXS data in this publication was analyzed by fitting key features associated with the bubble size and volume fraction using simple unified equations that combine well-known scattering approximations[42] and is detailed in our prior publication[7]. It is important to note that there are many other acceptable analyses that can be used to extract a size distribution of

bubbles from the data, which will all give similar volume-average bubble diameters. Following the methodology laid out in the initial characterization, a simple two-level unified equation could describe almost all of the SAXS data here:

$$I_{model}(q) = \left\{ \mathrm{G_1} \exp\left(\frac{-q^2 R_g^2}{3}\right) + \mathrm{B_1} \left[\frac{\left[\mathrm{erf}\left(\frac{qR_g}{\sqrt{6}}\right)\right]^3}{q} \right]^4 \right\} + \frac{\mathrm{B}_P}{q^4} + b \quad (1).$$

$$\mathrm{B_1} = \frac{G_1 4.86}{{R_g}^4} \quad (2).$$

where b is a flat background, G_1 is a scaling constant that is related to the contrast, size and total volume, B_p is the Porod constant of unknown, larger phases, and B_1 is calculated from G_1 and $\mathrm{R_g}$ and assumes a log-normal distribution of bubbles with a standard deviation of ≈ 0.3[43, 44]. Equation 1 is sufficient to describe the SAXS data when only one mode in the bubble size distribution is observed. It has been shown[7] that the smaller features (likely bubbles) are very heterogenous and often not observed. However, in cases where smaller features are above the background, b, an additional level is required, and the data are modeled by the equation:

$$I_{model}(q) = \left\{ \mathrm{G_1} \exp\left(\frac{-q^2 R_{g1}^2}{3}\right) + \mathrm{B_1} \left[\frac{\left[\mathrm{erf}\left(\frac{qR_{g1}}{\sqrt{6}}\right)\right]^3}{q} \right]^4 \right\} + \left\{ \mathrm{G_2} \exp\left(\frac{-q^2 R_{g2}^2}{3}\right) + \mathrm{B_2} \left[\frac{\left[\mathrm{erf}\left(\frac{qR_{g2}}{\sqrt{6}}\right)\right]^3}{q} \right]^4 \right\} + \frac{\mathrm{B}_P}{q^4} + b$$

$$\mathrm{B_2} = \frac{G_2 4.86}{{R_{g2}}^4}$$

where B_1 can now be fit to the data and B_2 is calculated. It is important to note that the presence of smaller features is only observable at high temperatures in the sample implanted with 0.1 % helium (>CB). Using the equation of state for helium [45] and the capillary approximation[46], the volume fraction of the mean-sized bubbles, v_B, and number density, N_B, can be estimated from the mean bubble radius, R_B, which is obtained from R_g by the relationship for spheres[47]. In cases where a size distribution is shown, the values of B, G and R_g are used to generate a log-normal distribution that is representative of the data[44]. In this manuscript, the volume-mean bubble size is reported to be consistent with the dominant features (location of the Guinier region) in the SAXS data, and the number-mode (obtained from the size distribution) is also reported for comparison with theory; for a log-normal distribution, the mode of the number distribution is also the median. The deviation in Porod scattering that is accounted for by an additional unified level in Equation 4 is treated as a separate population, but could also be accounted for with a core-shell model that would be qualitatively consistent with a transition region between the inner helium bubble and the surrounding Al matrix, as proposed by Caro et al.[48].

4. Results and Discussion

4.1 Bubble Morphology Characterization

The size distribution of the helium bubbles in the host metal is essential to predicting the alpha-irradiated material properties over time. Helium implanted aluminum (and many other metals) is well characterized by TEM here (Fig. 2a and Fig. 2b) and in the literature, with average bubble diameters, D_B, between 1 nm and 2 nm in ≈ 1 at. % implanted Al obtained from TEM images[49]. By comparison, SAXS is a volume-average technique where the signal is dominated by larger bubbles and in our previous study, a mean diameter from the volume distribution[7], $P_V(D_B)$, of ≈ 4 nm was reported with smaller bubbles (1 nm to 2 nm) that actually dominate the number distribution, $P_N(D_B)$; the volume-average is the mean value of the volume distribution, $P_V(D_B)$, which is $P_N(D_B)$ multiplied by the bubble volume, $V(D_B)$[7]. In order to establish consistency between SAXS and TEM, the number distributions, $P_N(D_B)$, obtained by SAXS, via the unified equation[44], are compared with TEM[6]. The bubble diameters observed by TEM are well within the $P_N(D_B)$ functions obtained from two different regions of an implanted sample where the helium loading differed by a factor of 2 (Fig. 2c). In general, bubble diameters between 1.5 nm and 4 nm are observed in the number distribution (Fig. 2c), which is consistent with the number distribution obtained by SAXS in the initial characterization[7] and other reports on aluminum[49]. Moreover, no distinguishable difference in the size distribution could be observed by TEM before and after annealing at 200 °C (Fig. 2b); SAXS measurements will show that a small fraction of large bubbles is present after annealing.

4.2 Bubble Dynamics at Temperature

The sensitivity of the implantation on the bubble size distribution can be observed qualitatively in the SAXS data at room temperature in Fig. 3a and Fig. 3c, and quantitatively in Fig. 3b and Fig. 3d. One might expect the slight increase in the mean bubble size to be due to the increase in helium concentration from 0.1 at. % (Fig 2a) to 0.2 at. % (Fig. 3c). However, the size distribution obtained from the radial position corresponding to 0.1 at. % from the sample implanted below the coulomb barrier (Fig. 2c) has a number-mode ≈3 nm that is still considerably larger than 2 nm observed in Fig. 3b. These differences in size distributions are outside of experimental error and highlight the importance of measuring a statistically significant number of bubbles and the influence of helium implantation conditions.

In situ SAXS measurements of the helium bubbles in both samples (Figs. 3a and 3c) reveal two distinct growth regimes at low and high temperatures. Low-temperature annealing (< 300 °C) does not significantly change the initial mean bubble size, which is in agreement with prior *ex situ* works[8],[9, 10]. Even when the temperature is held for four hours at 200 °C, the Guinier "knee", associated with bubble size, only decreases in intensity, but does not shift in q (Fig. S1a), suggesting that these bubbles decrease in number only (Fig. S1c). The decrease in the number of bubbles at 200 °C, coincides with an increase in the scattering at $q \approx 0.02$ Å^{-1} (Figs. S3 and S4), which suggests larger bubbles form at the expense of a small fraction of the smaller bubbles in both samples. This small fraction of bubble growth is difficult to resolve *in situ* because of changes in the X-ray scattering from grain boundaries in the host metal that is appreciable at low-q (Fig. S4). Instead, the scattering from these larger bubbles is more clearly observed with *ex situ* SAXS and is shown further in this manuscript; these larger bubbles are a very small fraction and thus also difficult to observe by TEM (Fig. 2b). By comparison, the sudden increase in the bubble size at 400 °C (Figs. 3a and Fig. S6) and 500 °C (Fig. 3c) is clear and indicates that a difference of 100 °C in the growth activation temperature, T_{crit}, is observed between the two

samples. In both samples, two different kinds of growth are observed during annealing: 1) growth of a small fraction of large (≈30 nm) bubbles that occurs at $T \geqq 200$ °C and 2) growth of a much larger volume fraction of bubbles, which is only activated at higher temperatures and depends strongly on the initial bubble morphology and implantation conditions.

Insight into the bubble dynamics at $T>T_{crit}$ can be gained by applying known bubble growth relationships to the observations in Fig. 3. At short-time scales, growth by dislocation loop punching is expected to occur, and modelled using both molecular dynamics and the analytical equation for the critical radius for dislocation loop punching[50], r_{DLP}. Molecular dynamics simulations of a system of four, 4 nm over-pressured bubbles (with a similar number density observed *in situ*) were carried out to simulate how the bubbles might grow during a temperature ramp to 800 K (Fig. 4) and how far the dislocations protruded from the surface. In these experiments, the helium bubbles were grown to 4 nm by increasing the number of atoms to obtain the correct pressure; this procedure resulted in dislocation loops at 300 K (Fig. 3), which are not expected to appreciably interfere with each other. Importantly, very little bubble growth is observed between 300 K and 800 K (Fig. 4). Therefore, the bubble growth observed above 4 nm in Figs. 3b and 3d is likely due to bubble-bubble growth mechanisms.

The critical radius for dislocation loop punching at each temperature was also calculated and compared to the MD results by finding the root to the equation[51]:

$$P(T, r_{DLP}) - P(298, r_{DLP}) = \frac{\mu b \ln {}^{r_{DLP}}/_{b}}{2\pi r_{DLP}} \quad (5).$$

where the term on the left represents the isochoric pressure increase of the bubble with radius, r_{DLP}, to temperature, T, which is calculated using the capillary approximation and the EOS of helium[50]. The right side is the growth term, above which, growth is expected and depends on the shear modulus of aluminum[52], μ, and the Burgers vector, b, calculated as function of temperature[53]. The root of equation (1) is the maximum radius where growth is expected by dislocation loop punching, r_{DLP}, at temperature, T, and is shown (scaled by a factor of 2 for diameter) in Figs. 3b and 3d with the experimental observations of the volume-mean bubble diameter and the number-mode bubble diameter. While the critical diameter for dislocation loop punching, D_{DLP}, is always smaller than the volume-mean diameter, it trends well with the number-mode, suggesting that Equation (5) accurately predicts differences in T_{crit} observed in Figs. 3b and 3d based on the initial bubble size alone. Values of D_{DLP} are also in good agreement with MD, which reveals minimal growth of 4 nm bubbles up to 525 °C. However, the continued growth at temperatures held above 400 °C deviates significantly from D_{DLP} and suggests another mechanism for bubble growth (e.g. bubble-bubble growth).

The magnitude of bubble growth at temperatures held above T_{crit} is greater than Equation (5) and MD after ≈ 45 minutes. Bubble-bubble growth mechanisms[54]·[55] considered here (Fig. 3e) are discernable via the temporal behavior of the mean diameter, $\overline{D_B}$, and number density, N_B, which have power-law dependencies that follow the relationships[56]:

$$\overline{D_B} = C + Bt^{1/n} \quad (6).$$

$$N_B = C + Bt^{-2/n} \quad (7).$$

where C and B are scaling constants and n = 2, 4 and 5 for Ostwald ripening [13], migration coalescence[57, 58] with volume diffusion and migration coalescence with surface diffusion,

respectively. Applying these relationships to the data in Fig. 3e reveals that the long-term bubble growth at temperature is best described by a migration coalescence and not Ostwald ripening in the sample with the smaller bubbles that are higher in number (0.1 at. %, 74 μm thick); agreement with the surface diffusion model is also somewhat better than that with volume diffusion. However, the time evolution in bubble size from 450 °C to 500 °C in the temperature ramp experiments from the sample with larger bubbles that are fewer in number (Fig. S8) reveal that both *B* and *n* are lower, with *n* approaching a value of 2, suggesting a difference in the growth mechanism and reduction in the growth kinetics. It is possible that the larger bubbles present at a higher helium concentration (and displacement damage) may be located at grain boundaries[59], which would reduce their mobility. While Ostwald ripening has been reported to be the dominant growth mechanism in implanted stainless steel[54],[55, 56], which has a higher shear modulus compared to aluminum, it is not possible to conclude this mechanism in aluminum. As well, higher temperature annealing in stainless steel is known to favor Ostwald ripening[60],[61]. The higher number density and smaller bubble sizes, obtained by implanting above the coulomb barrier, not only changes the bubble growth kinetics, but may also change the growth mechanism. These results highlight the influence of the implantation conditions on bubble growth kinetics.

4.3 Annealing Effects on Bubble Morphology and Bulk Properties

In addition to the changes in bubble sizes observed *in situ*, irreversible morphological changes to the helium bubbles are observed from *ex situ* SAXS measurements of annealed and non-annealed pieces. In these *ex situ* SAXS experiments, the small fraction of larger bubbles that were only faintly observed in the *in-situ* USAXS data are clearly observed within the full-width-at-half-maximum, FWHM, of the implant area (Fig. 5a). Furthermore, the original size distribution, prior to annealing, is observed in the sample that has been annealed at 500 °C for ≈4 hours, indicating that most of the bubbles grown in the experiments of Fig. 3e eventually relax back to their original size at room temperature after ≈ 2 months. This phenomenon is very likely to be specific to the implant conditions, host material and length of annealing time, as most bubbles implanted at 450 °C in ODS steel were much larger in size to those measured from a room temperature implant, measured by SAXS[62]. Other systems have shown similar results whereby a bimodal size distribution of bubbles was observed after annealing implanted nickel at 850 °C[63]. Reversibility in size of most bubbles has not been reported, suggesting that the larger bubbles formed at 500 °C (Fig. 3e) are not stable at lower temperatures. The *in situ* measurements taken for 2 hours after the temperature ramp experiments indicate that bubbles immediately shrink by ≈ 5 % when cooled to room temperature (Fig. S7) but take much longer (up to 2 months) to return to their original size. These results highlight how bubble sizes, necessary for prediction models, are highly dependent on the thermal history and the temperature at which they are measured. Moreover, the spatial distribution in the number density of bubbles inherent to the implantation profile[7] is preserved on the millimeter scale, indicating that any migration of the bubbles during the four-hour annealing was limited to within, at most, a pixel size of a few hundred microns. Therefore, the larger (≈ 30 nm) bubbles are likely the result of local migration-coalescence.

The effects of the large bubbles on the host-material are provided by known relationships with bubble size and number, as well as dislocation dynamics simulations using these size

distributions obtained by the *ex situ* SAXS data in Fig. 4; details of these simulations can be found in the supporting information. To a first approximation, the Friedel-Kroupa-Hirsch (FKH) relationship can predict the increase in yield strength, $\Delta\sigma_{yield}$:

$$\Delta\sigma_{yield} = \sum \frac{1}{8} M\mu b D_i N_i^{2/3} \quad (8).$$

where M is the Taylor factor (3.06 for Al), b is the magnitude of Burgers vector and D_i and N_i are diameter and number density of bubbles in the i^{th} bin of the number distribution[64]. Equation (8) predicts an increase in the yield strength and dislocation density when helium bubbles are present, which is also observed in dislocation dynamics (Figs. 6a and 6b). However, the change in yield strength before and after annealing is less clear. From Equation 4, the magnitude of $\Delta\sigma_{yield}$ is ≈ 3 % higher for the unannealed sample (400 MPa) compared with the bimodal size distribution of the annealed sample (390 MPa). This apparent decrease in yield strength with temperature arises from higher number density of bubbles in the unannealed sample, as the larger bubbles are not present in sufficient number to change $\Delta\sigma_{yield}$. On the other hand, very little difference in the yield strength is observed by dislocation dynamics (Fig. 6c). This discrepancy may be due to small number of larger bubbles present in the simulation or a reduction of velocity of dislocations near the bubbles. Importantly, dislocation dynamics reveals a significantly higher dislocation density with the larger bubbles (Fig. 6d), which may affect further bubble growth, for either dislocation loop punching[11] or migration. Therefore, the large bubbles have little effect on the yield strength but may affect subsequent bubble growth.

Comparison between MD and SAXS reveal some agreement, as well as highlight the need for future work. Specifically, the bubble growth mechanism at longer time-scales and the helium to vacancy ratio within the bubbles, He/Vac. Since MD uses explicit time integration with a time step that is a fraction of the atomic vibration period (for helium atoms), the simulated time is limited to tens of nanoseconds or perhaps up to about a microsecond in a heroic calculation. Simulations of bubble evolution on the longer time scales of the experiment require a different technique, such as accelerated molecular dynamics[34] or kinetic modeling such as mean field rate equations[65-68]. Applying these techniques to aluminum with helium bubbles requires substantial development and remains for future work. Using the surface tension obtained from MD, He/Vac can be estimated from the bubble size, D_B, in Figure 3 and compared with MD. Following the procedure outlined previously[7], the pressure can be estimated using the capillary approximation and the molar volume calculated using an appropriate equation of state for helium[46, 69]; details can be found in the supporting information. For the 0.2 at. % sample (<CB), the He/Vac values from the mode of the number distribution (3 nm) and mean of the volume distribution (6 nm) at room temperature in Figure 3 are 1.1 and 0.9, respectively; slightly larger values of 1.47 and 1.1 were obtained from the sample implanted at 0.1 at. % (>CB), respectively (Figure S10). These values are slightly less than 1.57, obtained from the 4 nm bubbles in MD at room temperature due to the way the nanobubbles are grown in MD. As the temperature is ramped to 550 ºC, the values of He/Vac for the mode of the number distribution and mean of the volume distribution decrease to ≈ 0.4 and 0.7, respectively in both samples. These values are of course considerably lower than 1.51 obtained at 900 K in MD, as the bubbles do not have time to grow as large in MD at high temperatures and remain at ≈ 4nm. Future work aimed at simulating bubble dynamics on longer time scales is likely to resolve the discrepancy at higher temperatures.

Conclusions

Based on these results, the critical bubble growth temperature, T_{crit}, is a key characteristic of a material exposed to alpha-radiation damage. Below this temperature, only a slight increase in the number of large, 30 nm, bubbles may be observed, while most of the original bubble sizes remain. As the temperature increases above T_{crit}, an immediate increase in the mean bubble size is observed in most all bubbles and is associated with both dislocation loop punching and bubble-bubble interactions. While at these higher temperatures, bubble growth is much faster in the sample with a higher number density of bubbles and characteristic of migration-coalescence. These results demonstrate how the bubble growth kinetics are strongly influenced by the initial bubble morphology and temperature. After cooling, most of the bubbles grown at 500 °C return to their original size, with only a small fraction of ≈30 nm bubbles observed, which have a minimal effect on the yield strength.

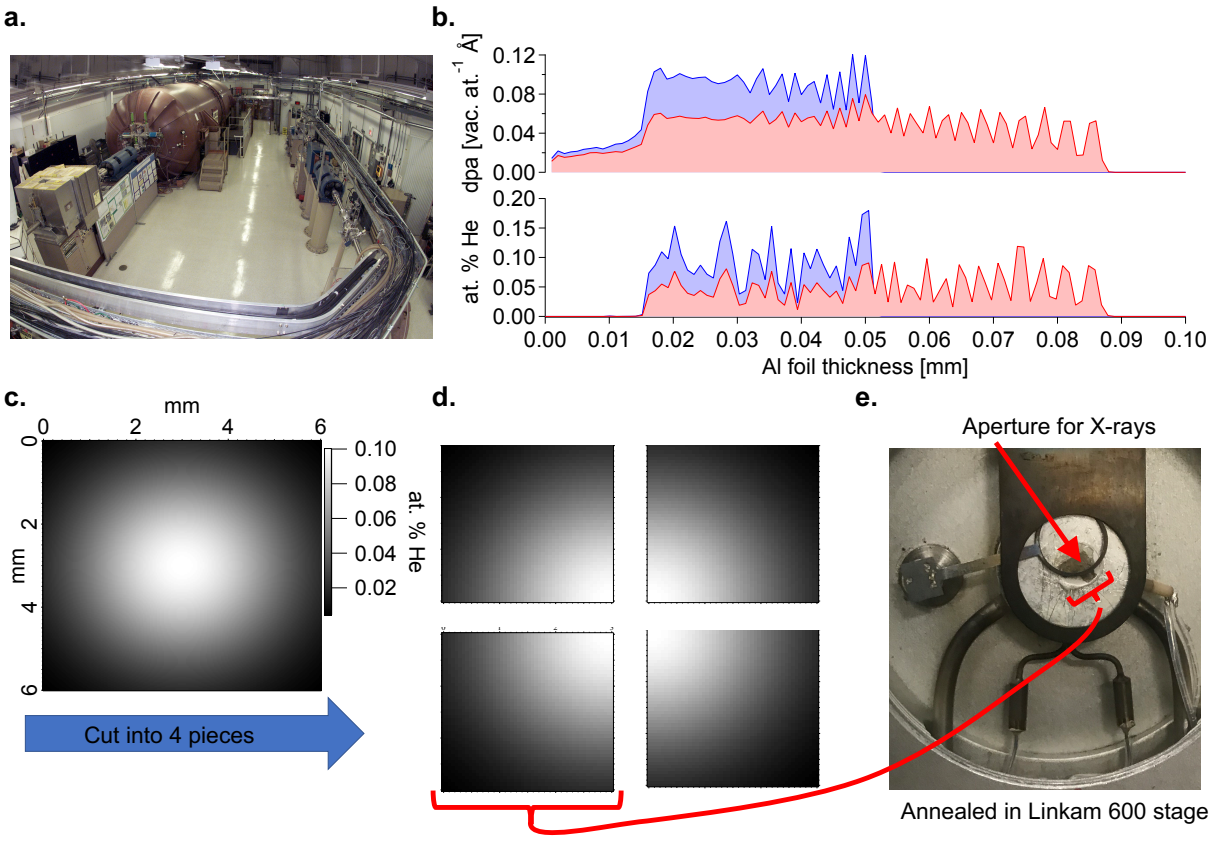

Fig. 1 | An illustration of how the different samples were implanted with He concentration that varied in the as-implanted sample, which was then cut into four pieces. Each piece was implanted at the CAMS facility at LLNL (a) using a range of energies and total measured charge that resulted in the helium concentration and displacement damage through the thickness of the Al shown in (b); these were estimated using SRIM. The ion beam profile used to implant the samples had a FWHM of ≈ 4 mm, which resulted in a radial gradient in He concentration (c). Each sample was cut into four pieces (d) that were used in either TEM measurements or X-ray

scattering experiments while annealing in a Linkam 600 heating stage (e); only the sample implanted with 0.1 % He is shown. In the X-ray experiments, the sample was positioned so that the X-ray aperture was within the FWHM of the He concentration profile (e).

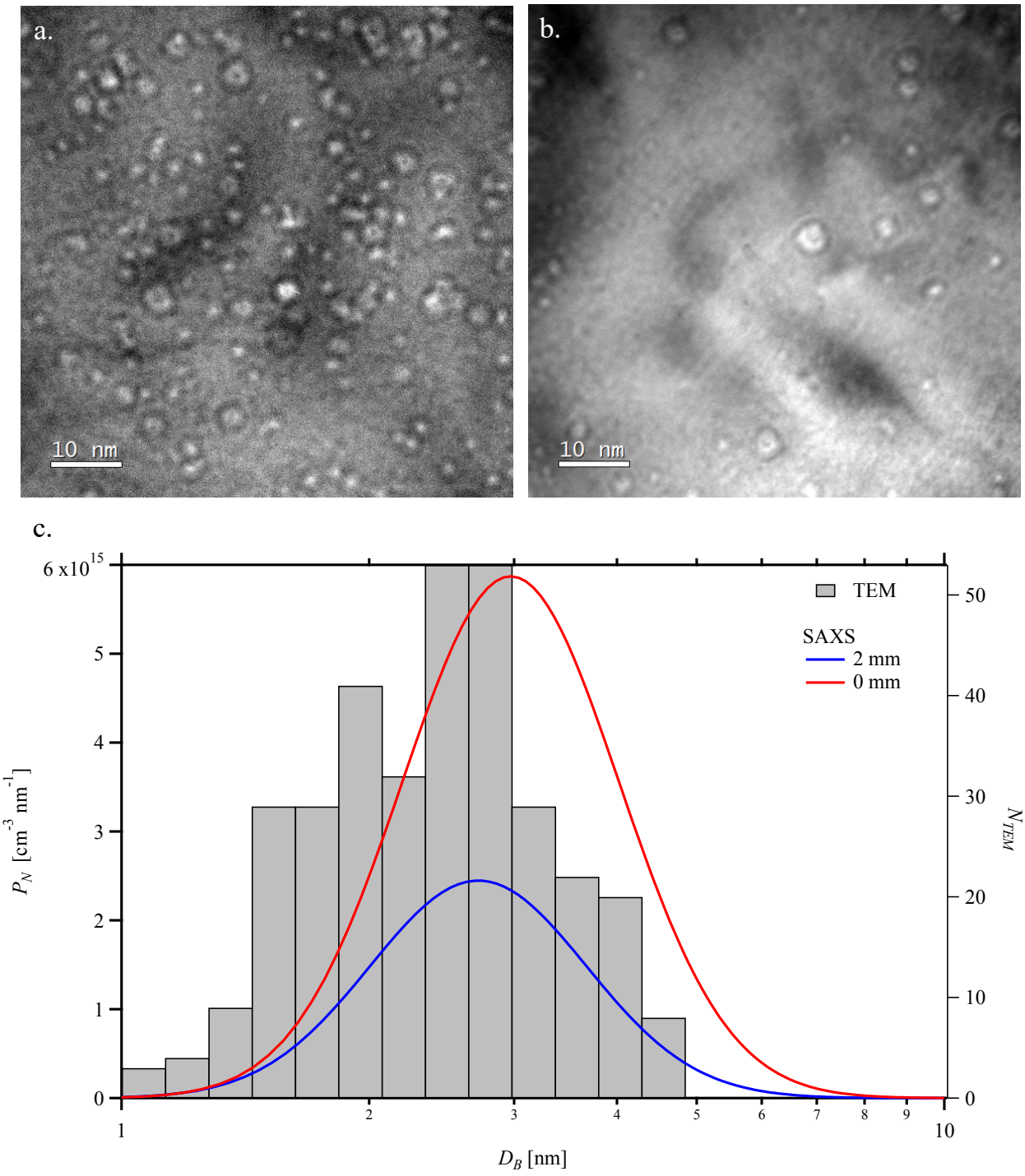

Fig. 2 | TEM images of the Al foil implanted with a peak He concentration of 0.2 % over 37 µm thickness and the corresponding size distribution. (a) A piece of the as-implanted foil, (b) a piece of the He implanted foil after annealing at 200 °C, (c) the number distribution obtained from 4 TEM images of the as-implanted sample (bars) along with the number distribution

obtained from the SAXS data from the as-implanted sample at the center (blue) and 2 mm away (red) where the concentration of implanted He is approximately half.

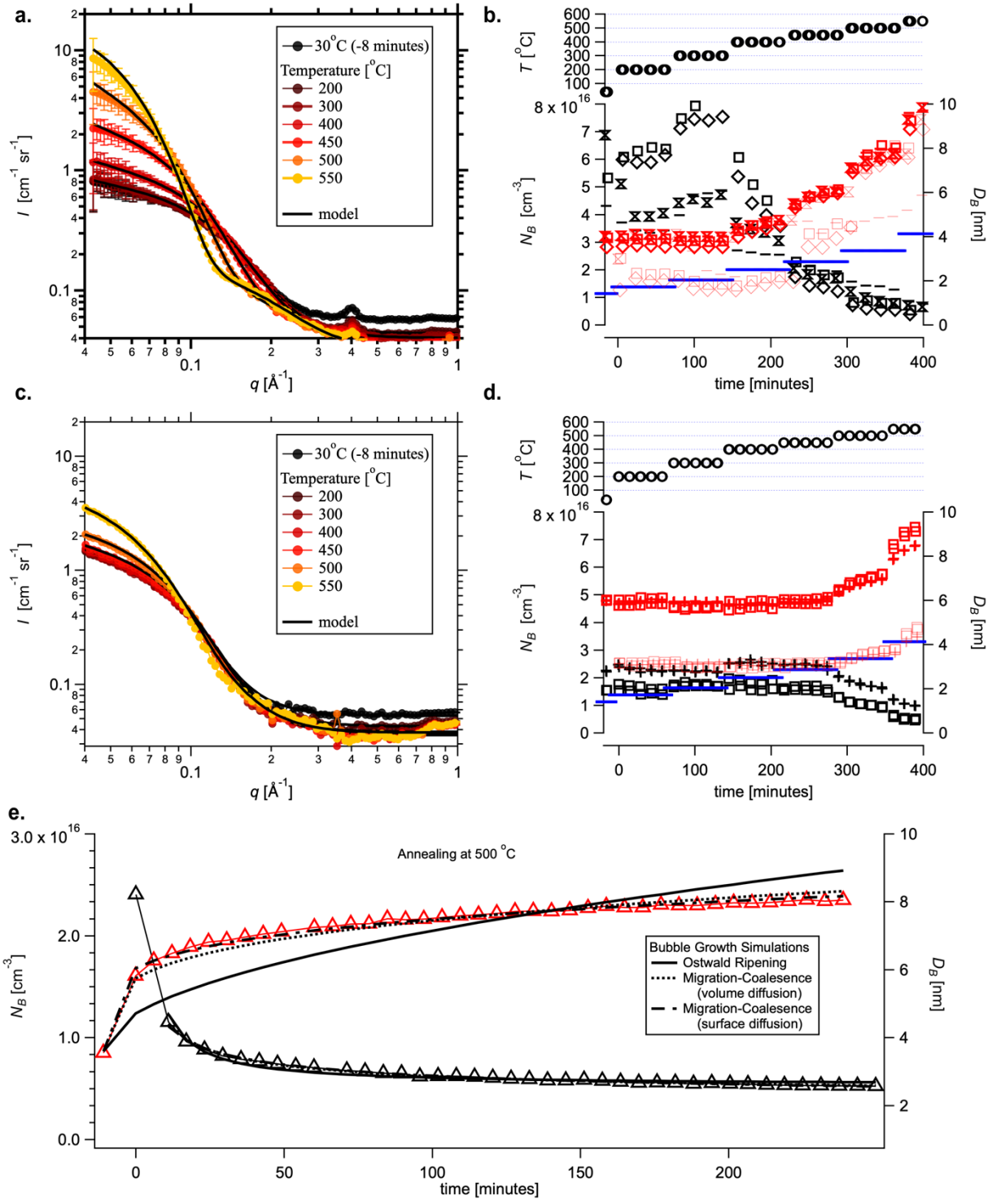

Fig. 3 | The in-situ SAXS results showing how the mean bubble diameter and number density evolve with time and temperature. The scattered intensity versus *q* of the SAXS data (markers)

and model fits of Equation 1 or Equation 2 (solid lines) obtained from the first frame collected at each temperature for the Al foil implanted with a peak He concentration of 0.1 % and 74 µm thickness (a). The bubble number density within the implanted region of each specific foil, N_B, (black) and the volume mean bubble diameter, D_B, (dark red) and the mode-Diameter of the number distribution (light red), obtained from the model fits, are shown in (b) for different regions of the implanted foil denoted by the "cross" markers for the high He concentration, and "circle" at 0.4 mm away (≈ 10 % reduction). A clear increase in the growth activation temperature is also observed from the Al foil implanted, below the coulomb barrier, with a peak He concentration of 0.2 % and 37 µm thickness (c). Analogous modeling results from (c) are shown in Fig. (d) for the high He concentration (crosses), "circles" at 0.4 mm away (≈10% reduction), "squares" at 0.6 mm away (≈15 % reduction) and "diamond" 0.8 mm away (≈20% reduction). The threshold diameter for dislocation loop punching is shown in blue lines for each temperature. The time evolution of the mode-diameter of the number distribution and number density observed during annealing of the high DPA foil at 500 °C are shown in (e) for longer periods of time (markers) and compared with what is expected from growth by Ostwald ripening (solid line), migration-coalesence via volume transport (dotted line) and migration-coalesence via surface transport (dashed line).

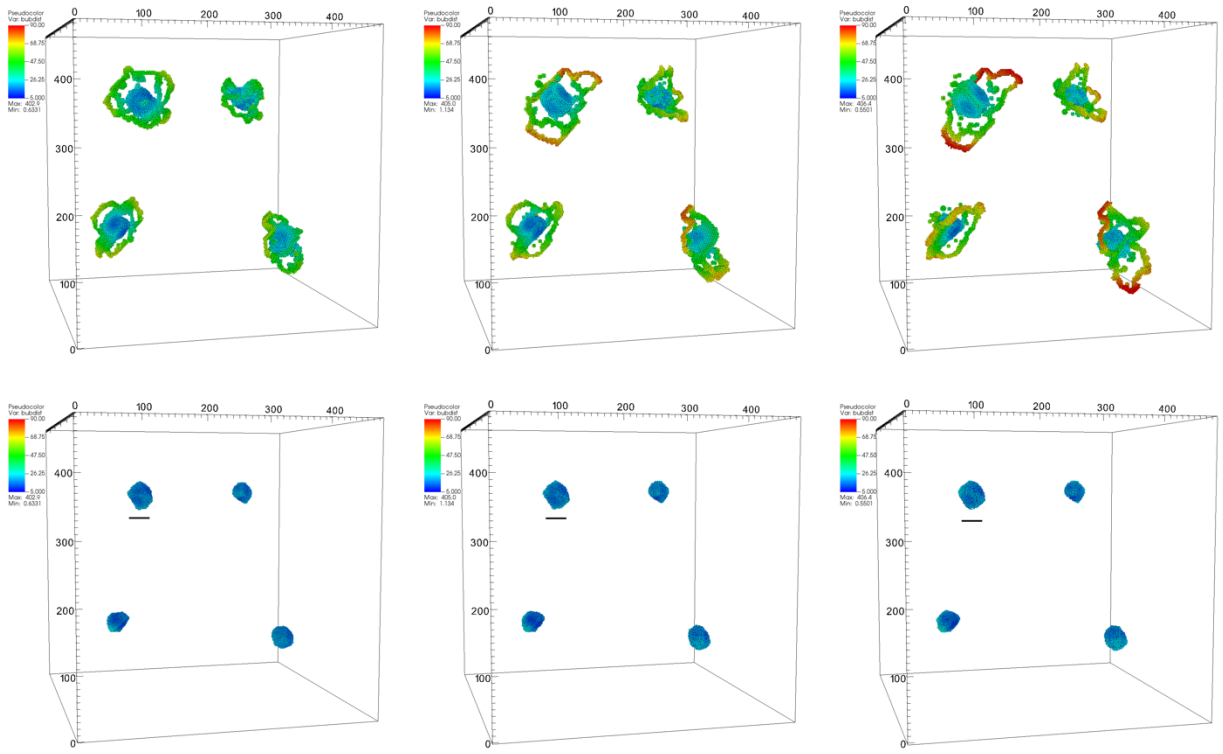

Fig. 4 | The molecular dynamics simulations of a system of four over pressurized He bubbles that have a size and number density consistent with the SAXS experiments in Fig. 2b for the low DPA sample. The top three panels show dislocations punched out by the bubble growth at temperature of 300K, 670K and 800K, from left to right. Only atoms in defects such as dislocation loops are plotted, and they are colored according to the distance from the center of

the bubble in Angstroms, as indicated in the legend. The lower panels are from the same simulation at the same time and temperature showing very little bubble growth with temperature. In these plots, only the helium atoms are shown to make the bubble size clearer. A black scale bar of 3 nm is placed below the upper left bubble in each of the three lower panels.

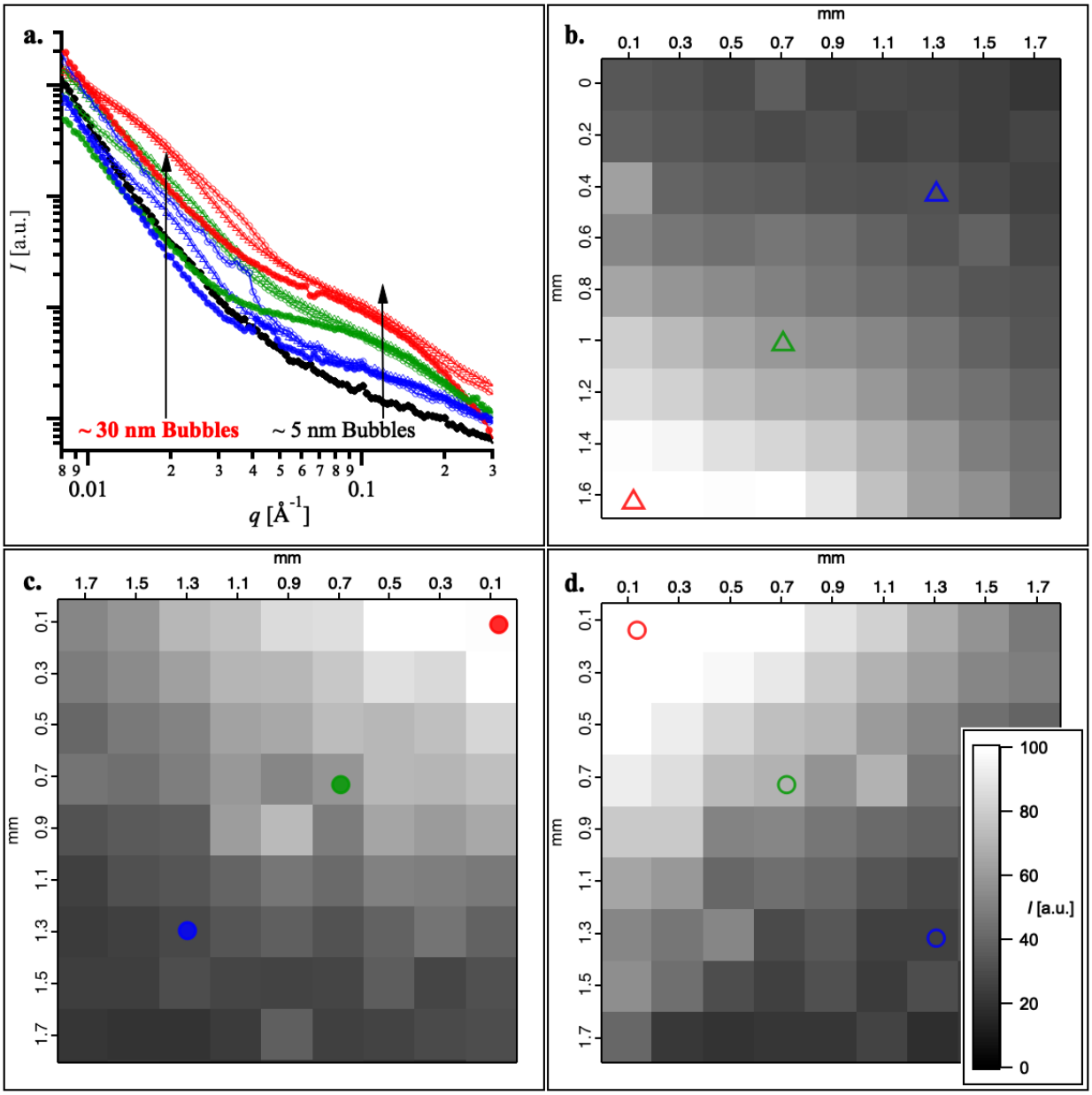

Fig. 5 | Ex situ SAXS data from the unannealed and annealed samples obtained across large areas of the samples. The log-log plot of SAXS data obtained from samples annealed at 500 °C (open triangles) and 200 °C (open circles) both have scattering from larger 30 nm bubbles compared with SAXS data obtained from the unannealed sample (closed circles) in (a). Maps of

the SAXS intensity at q = 0.11 Å^{-1} obtained from the He implanted Al foil one month after annealing at 500 °C (b), as-implanted (c) and after annealing at 200 °C (d) reveal the gradient in number density is preserved after annealing.

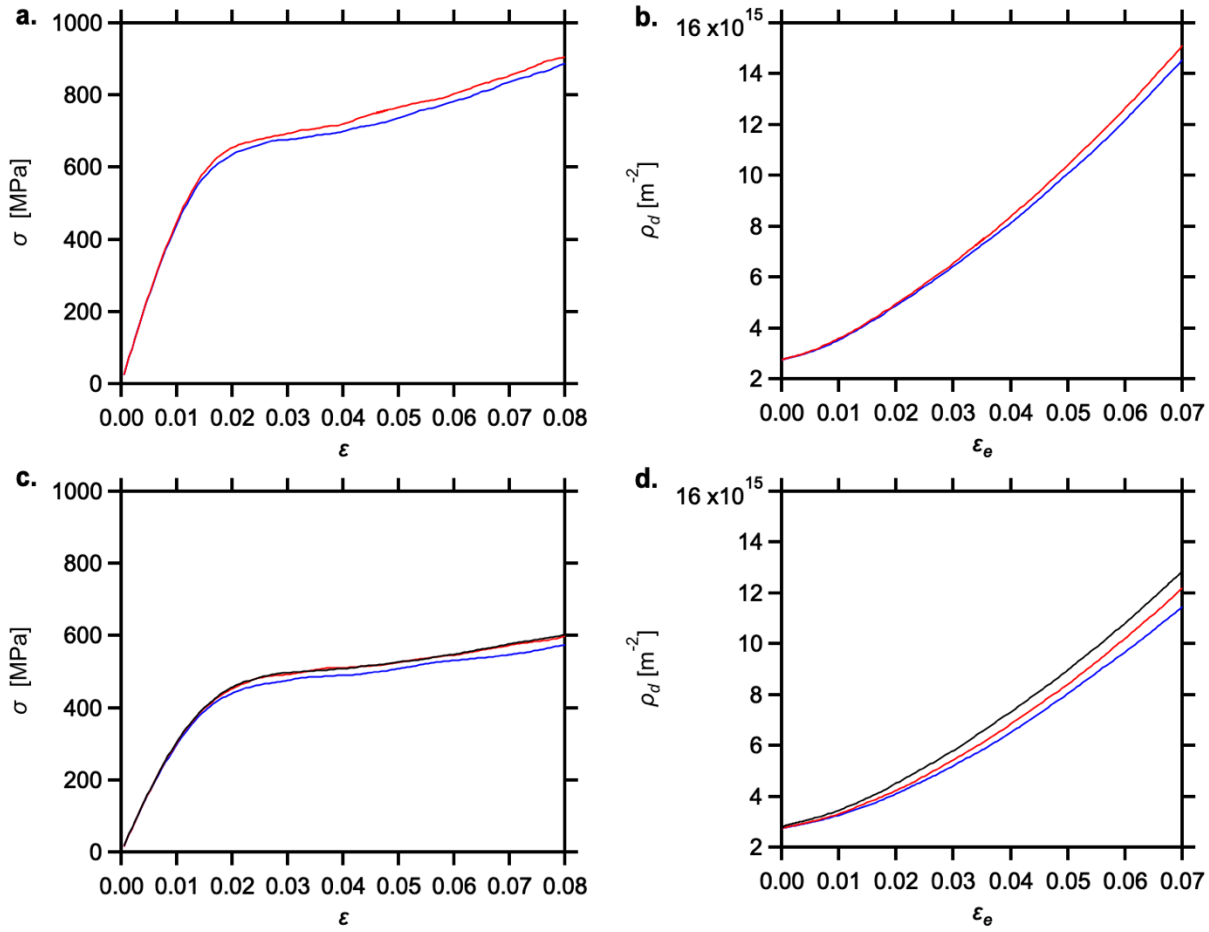

Fig. 6 | Dislocation dynamics simulations of aluminum with and without He bubbles. (a) Stress/strain relationships between pure aluminum (blue), and aluminum with bubbles (red) at 300K. The number density of bubbles corresponds to the un-annealed samples distribution (b) Dislocation density evolution comparisons without bubbles (blue), and with bubbles (red). (c) Stress/strain relationships between pure aluminum (blue), and aluminum with small bubbles only (red), and a combination of small and large bubbles (black) at 770K. The number density of bubbles corresponds to the presence of bubbles in the annealed samples. (d) Dislocation density evolution comparisons without bubbles (blue), with small bubbles (red), and with a combination of small and large bubbles (black).

Notes

ACKNOWLEDGMENT

This manuscript (LLNL-JRNL-818950) was prepared at the Lawrence Livermore National Laboratory under the auspices of the U.S. Department of Energy under Contract DE-AC52-07NA27344. This research used resources of the Advanced Photon Source (12-IDB and 9-IDC), a U.S. Department of Energy (DOE) Office of Science User Facility, operated for the DOE Office of Science by Argonne National Laboratory under Contract No. DE-AC02-06CH11357.

ABBREVIATIONS

SAXS, small angle x-ray scattering; XRD, x-ray diffraction; WAXS, wide angle X-ray scattering

References

[1] H. Schroeder, W. Kesternich, H. Ullmaier, Helium effects on the creep and fatigue resistance of austenitic stainless steels at high temperatures, Nuclear Engineering and Design. Fusion 2(1) (1985) 65-95.
[2] K. Farrell, Experimental effects of helium on cavity formation during irradiation—a review, Radiation Effects 53(3-4) (1980) 175-194.
[3] S.E. Donnelly, M. Renier, A.A. Lucas, H.J. Whitlow, Lateral stress-induced blistering of aluminium films under helium irradiation, J. Nucl. Mater. 115(2-3) (1983) 347-349.
[4] S.-H. Li, J.-T. Li, W.-Z. Han, Radiation-Induced Helium Bubbles in Metals, Materials 12(7) (2019).
[5] L.K. Mansur, W.A. Coghlan, Mechanisms of helium interaction with radiation effects in metals and alloys: A review, J. Nucl. Mater. 119(1) (1983) 1-25.

[6] J.R. Jeffries, J.A. Hammons, T.M. Willey, M.A. Wall, D. Ruddle, J. Ilavsky, P.G. Allen, T. van Buuren, Probing He bubbles in naturally aged and annealed delta-Pu alloys using ultra-small-angle x-ray scattering, J. Nucl. Mater. 498 (2018) 505-510.
[7] J.A. Hammons, S.J. Tumey, Y. Idell, J.R. Jeffries, He Bubble Concentration, Size and Strain in Implanted Aluminum by SAXS/WAXS, JOM 72(1) (2020) 176-186.
[8] C.L. Snead, A.N. Goland, F.W. Wiffen, TRACING EVOLUTION OF BUBBLES IN HELIUM-INJECTED ALUMINUM BY MEANS OF POSITRON-ANNIHILATION, J. Nucl. Mater. 64(1-2) (1977) 195-205.
[9] W. Bauer, G.J. Thomas, Helium implantation effects in SAP and aluminum, J. Nucl. Mater. 63 (1976) 299-306.
[10] K.L. Wilson, G.J. Thomas, Low-energy helium implantation of aluminum, J. Nucl. Mater. 63 (1976) 266-272.
[11] W.G. Wolfer, Dislocation loop punching in bubble arrays, Philos. Mag. A 59(1) (1989) 87-103.
[12] H. Trinkaus, W.G. Wolfer, Conditions for dislocation loop punching by helium bubbles, J. Nucl. Mater. 122(1) (1984) 552-557.
[13] G.W. Greenwood, A. Boltax, The role of fission gas re-solution during post-irradiation heat treatment, J. Nucl. Mater. 5(2) (1962) 234-240.
[14] P.J. Goodhew, S.K. Tyler, A. Kelly, Helium bubble behaviour in b. c. c. metals below 0.65Tm, Proceedings of the Royal Society of London. A. Mathematical and Physical Sciences 377(1769) (1981) 151-184.
[15] J.F. Ziegler, M.D. Ziegler, J.P. Biersack, SRIM – The stopping and range of ions in matter (2010), Nuclear Instruments and Methods in Physics Research Section B: Beam Interactions with Materials and Atoms 268(11) (2010) 1818-1823.
[16] J. Ilavsky, F. Zhang, R.N. Andrews, I. Kuzmenko, P.R. Jemian, L.E. Levine, A.J. Allen, Development of combined microstructure and structure characterization facility for in situ and operando studies at the Advanced Photon Source, J. Appl. Crystallogr. 51(3) (2018) 867-882.
[17] J. Ilavsky, P.R. Jemian, Irena: tool suite for modeling and analysis of small-angle scattering, J. Appl. Crystallogr. 42 (2009) 347 – 353.
[18] J. Ilavsky, Nika: software for two-dimensional data reduction, J. Appl. Crystallogr. 45(2) (2012) 324 – 328.
[19] A. Arsenlis, W. Cai, M. Tang, M. Rhee, T. Oppelstrup, G. Hommes, T.G. Pierce, V.V. Bulatov, Enabling strain hardening simulations with dislocation dynamics, Modell. Simul. Mater. Sci. Eng. 15(6) (2007) 553-595.
[20] S. Aubry, S. Queyreau, A. Arsenlis, Dislocation Dynamics Modeling of the Interaction of Dislocations with Eshelby Inclusions, Mechanics and Physics of Solids at Micro- and Nano-Scales (2019) 55-85.
[21] F. Ercolessi, J.B. Adams, INTERATOMIC POTENTIALS FROM 1ST-PRINCIPLES CALCULATIONS - THE FORCE-MATCHING METHOD, Europhys. Lett. 26(8) (1994) 583-588.
[22] D.E. Beck, INTERATOMIC POTENTIALS FOR HELIUM AND MOLECULES OF HELIUM ISOTOPES, J. Chem. Phys. 50(1) (1969) 541-&.
[23] S. Plimpton, Fast Parallel Algorithms for Short-Range Molecular Dynamics, Journal of Computational Physics 117(1) (1995) 1-19.

[24] R.E. Rudd, Void growth in bcc metals simulated with molecular dynamics using the Finnis–Sinclair potential, Philosophical Magazine 89(34-36) (2009) 3133-3161.
[25] E.T. Seppälä, J. Belak, R.E. Rudd, Effect of stress triaxiality on void growth in dynamic fracture of metals: A molecular dynamics study, Phys. Rev. B 69(13) (2004) 134101.
[26] R.E. Rudd, J.F. Belak, Void nucleation and associated plasticity in dynamic fracture of polycrystalline copper: an atomistic simulation, Computational Materials Science 24(1) (2002) 148-153.
[27] M.R. Gungor, D. Maroudas, S. Zhou, Molecular-dynamics study of the mechanism and kinetics of void growth in ductile metallic thin films, Appl. Phys. Lett. 77(3) (2000) 343-345.
[28] L. Li, L. Peng, J. Shi, W. Jiang, Large helium-vacancy clusters coalescence during helium bubble evolution under cascade in iron with edge dislocation: A MD simulation, Computational Materials Science 197 (2021) 110601.
[29] A. Weerasinghe, B.D. Wirth, D. Maroudas, Elastic Properties of Plasma-Exposed Tungsten Predicted by Molecular-Dynamics Simulations, ACS Applied Materials & Interfaces 12(19) (2020) 22287-22297.
[30] A.Y. Hamid, J. Sun, H. Zhang, A.S. Jadon, T. Stirner, Molecular dynamics simulations of helium clustering and bubble growth under tungsten surfaces, Computational Materials Science 163 (2019) 141-147.
[31] K.D. Hammond, S. Blondel, L. Hu, D. Maroudas, B.D. Wirth, Large-scale atomistic simulations of low-energy helium implantation into tungsten single crystals, Acta Mater. 144 (2018) 561-578.
[32] L. Yang, F. Gao, R.J. Kurtz, X.T. Zu, S.M. Peng, X.G. Long, X.S. Zhou, Effects of local structure on helium bubble growth in bulk and at grain boundaries of bcc iron: A molecular dynamics study, Acta Mater. 97 (2015) 86-93.
[33] R.D. Smirnov, S.I. Krasheninnikov, J. Guterl, Atomistic modeling of growth and coalescence of helium nano-bubbles in tungsten, J. Nucl. Mater. 463 (2015) 359-362.
[34] L. Sandoval, D. Perez, B.P. Uberuaga, A.F. Voter, Competing Kinetics and He Bubble Morphology in W, Phys. Rev. Lett. 114(10) (2015).
[35] L. Hu, K.D. Hammond, B.D. Wirth, D. Maroudas, Molecular-dynamics analysis of mobile helium cluster reactions near surfaces of plasma-exposed tungsten, J. Appl. Phys. 118(16) (2015) 163301.
[36] Y.L. Zhou, J. Wang, Q. Hou, A.H. Deng, Molecular dynamics simulations of the diffusion and coalescence of helium in tungsten, J. Nucl. Mater. 446(1) (2014) 49-55.
[37] G. Lucas, R. Schäublin, Stability of helium bubbles in alpha-iron: A molecular dynamics study, J. Nucl. Mater. 386-388 (2009) 360-362.
[38] J. Pu, L. Yang, X.T. Zu, F. Gao, A molecular dynamics study of helium bubble stability during high-energy displacement cascades in α-iron, Physica B: Condensed Matter 398(1) (2007) 65-70.
[39] J. Marian, J. Knap, M. Ortiz, Nanovoid Cavitation by Dislocation Emission in Aluminum, Phys. Rev. Lett. 93(16) (2004) 165503.
[40] Y. Mishin, D. Farkas, M.J. Mehl, D.A. Papaconstantopoulos, Interatomic potentials for monoatomic metals from experimental data and ab initio calculations, Phys. Rev. B 59(5) (1999) 3393-3407.
[41] F. Ercolessi, J.B. Adams, Interatomic Potentials from First-Principles Calculations: The Force-Matching Method, Europhysics Letters (EPL) 26(8) (1994) 583-588.

[42] G. Beaucage, Approximations leading to a unified exponential power-law approach to small-angle scattering, J. Appl. Crystallogr. 28 (1995) 717-728.
[43] B. Hammouda, A new Guinier-Porod model, J. Appl. Crystallogr. 43 (2010) 716-719.
[44] G. Beaucage, H.K. Kammler, S.E. Pratsinis, Particle size distributions from small-angle scattering using global scattering functions, J. Appl. Crystallogr. 37(4) (2004) 523-535.
[45] R.L. Mills, D.H. Liebenberg, J.C. Bronson, Equation of state and melting properties of He4 from measurements to 20 kbar, Phys. Rev. B 21(11) (1980) 5137-5148.
[46] S.E. Donnelly, The density and pressure of helium in bubbles in implanted metals: A critical review, Radiation Effects 90(1-2) (1985) 1-47.
[47] A. Guinier, G. Fournet, Small-angle scattering of X-rays, Wiley, New York,, 1955.
[48] A. Caro, D. Schwen, E. Martinez, Structure of nanoscale gas bubbles in metals, Appl. Phys. Lett. 103(21) (2013).
[49] S.R. Soria, A. Tolley, E.A. Sanchez, The influence of microstructure on blistering and bubble formation by He ion irradiation in Al alloys (vol 467, pg 357, 2015), J. Nucl. Mater. 469 (2016) 269-269.
[50] D.A. Gyorog, E.F. Obert, VIRIAL COEFFICIENTS FOR ARGON, METHANE, NITROGEN, AND XENON, AlChE J. 10(5) (1964) 621-625.
[51] G.W. Greenwood, A.J.E. Foreman, D.E. Rimmer, The role of vacancies and dislocations in the nucleation and growth of gas bubbles in irradiated fissile material, J. Nucl. Mater. 1(4) (1959) 305-324.
[52] J.L. Tallon, A. Wolfenden, Temperature dependence of the elastic constants of aluminum, J. Phys. Chem. Solids 40(11) (1979) 831-837.
[53] N.H.N. Philip, The Crystallography of Aluminum and Its Alloys, Encyclopedia of Aluminum and Its Alloys, CRC Press2018.
[54] J. Rothaut, H. Schroeder, H. Ullmaier, The growth of helium bubbles in stainless steel at high temperatures, Philosophical Magazine A: Physics of Condensed Matter, Structure, Defects and Mechanical Properties 47(5) (1983) 781-795.
[55] I. Villacampa, J.C. Chen, P. Spätig, H.P. Seifert, F. Duval, Helium bubble evolution and hardening in 316L by post-implantation annealing, J. Nucl. Mater. 500 (2018) 389-402.
[56] A.M. Ovcharenko, I.I. Chernov, On the theory of bubble coarsening in metals, J. Nucl. Mater. 528 (2020) 151824.
[57] G.W. Greenwood, M.V. Speight, An analysis of the diffusion of fission gas bubbles and its effect on the behaviour of reactor fuels, J. Nucl. Mater. 10(2) (1963) 140-144.
[58] E.E. Gruber, Calculated Size Distributions for Gas Bubble Migration and Coalescence in Solids, J. Appl. Phys. 38(1) (1967) 243-250.
[59] F. Zhang, X. Wang, J.B. Wierschke, L. Wang, Helium bubble evolution in ion irradiated Al/B4C metal metrix composite, Scripta Mater. 109 (2015) 28-33.
[60] G.A. Sun, E.D. Wu, C.Q. Huang, C. Cheng, G.Y. Yan, X.L. Wang, S. Liu, Q. Tian, B. Chen, Z.H. Wu, Y. Liu, J. Wang, Evolution and change of He bubbles in He-containing Ti films upon thermal treatment studied by small-angle X-ray scattering and transmission electron microscopy, Thin Solid Films 558 (2014) 125-133.
[61] M.L. Sattler, W.A. Jesser, Microstructural contributions to bubble growth in helium ion irradiated nickel, J. Nucl. Mater. 122(1-3) (1984) 523-530.

[62] Y. Song, L. Song, T. Zhu, Y. Chen, S. Jin, F. Tian, Z. Hong, P. Zhang, B. Wang, H. Wang, Q. Yan, F. Bian, X. Cao, The investigation of distribution on size and concentration of helium bubbles in Y-bearing ODS steel using by SAXS and GIXRD, J. Nucl. Mater. 554 (2021) 153083.
[63] D. Schwahn, H. Ullmaier, J. Schelten, W. Kesternich, Gas densities in he bubbles and their size distribution in nickel measured by neutron scattering, Acta Metall. 31(12) (1983) 2003-2011.
[64] S.J. Zinkle, Y. Matsukawa, Observation and analysis of defect cluster production and interactions with dislocations, J. Nucl. Mater. 329-333 (2004) 88-96.
[65] S. Taller, G. VanCoevering, B.D. Wirth, G.S. Was, Predicting structural material degradation in advanced nuclear reactors with ion irradiation, Scientific Reports 11(1) (2021) 2949.
[66] A.A. Kohnert, B.D. Wirth, L. Capolungo, Modeling microstructural evolution in irradiated materials with cluster dynamics methods: A review, Computational Materials Science 149 (2018) 442-459.
[67] J. Marian, C.S. Becquart, C. Domain, S.L. Dudarev, M.R. Gilbert, R.J. Kurtz, D.R. Mason, K. Nordlund, A.E. Sand, L.L. Snead, T. Suzudo, B.D. Wirth, Recent advances in modeling and simulation of the exposure and response of tungsten to fusion energy conditions, Nucl. Fusion 57(9) (2017) 092008.
[68] G.-H. Lu, H.-B. Zhou, C.S. Becquart, A review of modelling and simulation of hydrogen behaviour in tungsten at different scales, Nucl. Fusion 54(8) (2014) 086001.
[69] P.G. Allen, W.G. Wolfer, Generalized Rate Theory for Void and Bubble Swelling and its Application to Plutonium Metal Alloys, United States, 2015, p. 22.